fibers

MDPI

Article

Amplifying the Sensitivity of Electrospun Polyvinylidene Fluoride Piezoelectric Sensors Through Electrical Polarization Process for Low-Frequency Applications

Asra Tariq, Amir H. Behravesh, Muhammad Tariq and Ghaus Rizvi *

Faculty of Engineering and Applied Science, Ontario Tech University, Oshawa, ON L1G0C5, Canada; asra.tariq@ontariotechu.net (A.T.)
* Correspondence: ghaus.rizvi@ontariotechu.ca

Abstract: Piezoelectric sensors convert mechanical stress into electrical charge via the piezoelectric effect, and when fabricated as fibers, they offer flexibility, lightweight properties, and adaptability to complex shapes for self-powered wearable sensors. Polyvinylidene fluoride (PVDF) nanofibers have garnered significant interest due to their potential applications in various fields, including sensors, actuators, and energy-harvesting devices. Achieving optimal piezoelectric properties in PVDF nanofibers requires the careful optimization of polarization. Applying a high electric field to PVDF chains can cause significant mechanical deformation due to electrostriction, leading to crack formation and fragmentation, particularly at the chain ends. Therefore, it is essential to explore methods for polarizing PVDF at the lowest possible voltage to prevent structural damage. In this study, a Design of Experiments (DoE) approach was employed to systematically optimize the polarization parameters using a definitive screening design. The main effects of the input parameters on piezoelectric properties were identified. Heat treatment and the electric field were significant factors affecting the sensor's sensitivity and β-phase fraction. At the highest temperature of 120 °C and the maximum applied electric field of 3.5 kV/cm, the % β-phase (F(β)) exceeded 95%. However, when reducing the electric field to 1.5 kV/cm and 120 °C, the % F(β) ranged between 87.5% and 90%. The dielectric constant ($\mathcal{E}'$) of polarized PVDF was determined to be 30 at an electric field frequency of 1 Hz, compared to a value of 25 for non-polarized PVDF. The piezoelectric voltage coefficient (g_{33}) for polarized PVDF was measured at 32 mV·m/N at 1 Hz, whereas non-polarized PVDF exhibited a value of 3.4 mV·m/N. The findings indicate that, in addition to a high density of β-phase dipoles, the polarization of these dipoles significantly enhances the sensitivity of the PVDF nanofiber mat.

Keywords: electrospun sensor; polarization; piezoelectric; sensor sensitivity; β-phase

check for updates

Academic Editor: Mataz Alcoutlabi

Received: 4 November 2024
Revised: 5 December 2024
Accepted: 7 January 2025
Published: 9 January 2025

Citation: Tariq, A.; Behravesh, A.H.; Tariq, M.; Rizvi, G. Amplifying the Sensitivity of Electrospun Polyvinylidene Fluoride Piezoelectric Sensors Through Electrical Polarization Process for Low-Frequency Applications. *Fibers* **2025**, *13*, 5. https://doi.org/10.3390/fib13010005

Copyright: © 2025 by the authors. Licensee MDPI, Basel, Switzerland. This article is an open access article distributed under the terms and conditions of the Creative Commons Attribution (CC BY) license (https://creativecommons.org/licenses/by/4.0/).

1. Introduction

Advances in the sensing efficiency of nanomaterials have had a huge impact on microelectronics and flexible electronics for sensors. Nanomaterial-based sensors are increasingly transitioning from research laboratories to real-life applications, spanning industries and medicine. In medicine, nanomaterial-based sensors are enabling breakthroughs in diagnostics, wearable health monitoring, and early disease detection [1]. Electrospun nanofibers, with their inherent advantages of being lightweight, possessing high surface areas, and exhibiting excellent flexibility and conformability, are emerging as a promising material for sensors [2–4]. Nanofiber-based sensors usually generate electrical signals such as voltage,

current, capacitance, or resistance, etc., and these output signals guide and determine the principles of sensor design [5,6].

Piezoelectric sensors have been explored by researchers for a long time and many ceramic-based piezoelectric sensors (lead zirconate titanate) have been commercialized [7–11]. In addition to ceramic-based piezoelectric materials like lead zirconate titanate (PZT) and barium titanate ($BaTiO_3$), piezoelectric polymers such as polyvinylidene fluoride (PVDF) and its copolymers, as well as molecular ferroelectrics, are commonly explored for sensors. These materials can convert mechanical stimulations into electrical signals, usually voltage or charge generation. Piezoelectric sensors have found extensive application in wearable electronics due to their quick response times, high sensitivity, good linearity, wide dynamic range, wide frequency bandwidth, low power consumption, affordability, and ease of integration into devices [12]. In a recent work, Li et al. presented a novel electrostatic disc microprinting technique for printing PZT that aimed to overcome the challenges associated with fabricating piezoelectric elements, such as nanoparticles, films, and patterns [13]. However, it was observed that printed ink-based sensors often exhibit low mechanical integrity, requiring a stable substrate material for reliable performance. In such cases, ensuring strong, long-term interfacial adhesion between the printed ink and the substrate is crucial for maintaining sensor durability and function over time. Ferroelectric molecular crystals have also been explored by researchers for sensor applications. These materials are composed of organic molecules with inherent dipoles that can be aligned to induce macroscopic polarization. Yet, these materials have high brittleness because of their crystal nature, limiting their use in flexible or wearable sensor applications [14]. PVDF and its copolymers are highly flexible and, because of this, can easily bend and wrap around the wrist or curved body parts for biomechanical analysis [15]. One crucial challenge associated with PVDF is the substantial disorder of electric dipoles found in almost all bulk and thin-film samples. Additionally, PVDF exhibits five distinct crystalline structures, known as α, β, γ, δ, and ε phases [16]. The α-phase is the thermodynamically stable phase; however, it is not inherently piezoelectric because its molecular structure does not exhibit the necessary asymmetry required for piezoelectricity. In the α phase, the PVDF polymer chains are arranged in a trans–gauche chain conformation, resulting in the self-cancelation of dipoles [17,18]. The ε and δ phases are seldom studied due to their instability [19]. The β phase, having a polymer chain with a zigzag (all-trans) conformation (TTTT), is of particular interest. The content of the β phase (F(β)) is crucial, as the electroactive properties depend significantly on it.

Researchers have explored different methods to enhance the piezoelectric properties of PVDF. One approach involves converting the non-piezoelectric α-phase of PVDF into the piezoelectric β-phase through techniques such as stretching [20], thermal treatment [21], and or incorporating piezo-fillers [22,23]; another famous method involves poling the material under a high electric field [24,25]. Huang et al. showed a significant advancement in domain engineering by cyclic compression and rapid freezing for PVDF to achieve enhanced piezoelectric properties on the commercial scale [26]. Zhu et al. studied the effect of the thermal annealing process at different temperatures on the F(β) and dielectric properties ($\mathcal{E}'$) of PVDF. It was found that isothermal annealing at 140 °C for 6 h increased the degree of crystallinity from 37.5% to 46.2%. The F(β) was also enhanced remarkably from 49.8% to 80.3% [21]. Shobhneek et al. observed that the annealing of a solution-cast thick film of PVDF at more than 100 °C offers the maximum F(β) [18]. Salimi et al. examined the β-phase transformation in PVDF films and found that the highest F(β), reaching 74%, occurred in compression-molded PVDF films stretched at a ratio between 4.5 and 5 [27]. Debili et al. investigated the impact of stretching, the polarization temperature (60–120 °C), and electric field (300–700 kV/cm) on reversible α-to-β phase transformation

and the improvement of the piezoelectric coefficient (d_{33}) in PVDF nanofilms. During the quasi-static testing, a d_{33} value of 10 pC/N was achieved [28]. The enhancement of PVDF's piezoelectric properties through high-electric-field polarization operates through two mechanisms. Initially, the high electric field aligns the material's dipoles in the direction of the field, creating a net dipole moment within the material. Additionally, the high electric field can stimulate the formation of the β phase within PVDF. The alignment of dipoles induced by the electric field aids in the crystallization of PVDF into the β phase, resulting in an enhanced piezoelectric performance [29]. However, it was noticed that employing a very high electric field (8.7414×10^9 V/m) on PVDF chains can cause excessive mechanical deformation during the effect of electrostriction. Very strong electric field was observed to induce the crack and fragmentation of PVDF molecular chains, with the C-H and C-F bonds located usually at the ends of the molecular chain exhibiting the initial susceptibility to breakage [30]. From the above-mentioned literature, it was observed that most of the researchers polarized PVDF based film during processing or by doing post processing. It was also observed that the fabrication process used for making thin films of PVDF can affect the β-phase crystal and sensitivity [31–33]. For example, in the electrospinning process, the PVDF chains are stretched and intrinsically subjected to a high electric field that promotes β-phase generation [34,35]. Additionally, piezoelectric nanofibers provide a much higher surface area compared to continuous films, which enhances their sensitivity and responsiveness in applications like sensing and energy harvesting. The tape casting method and solvent casting provide less β-phase because the chains involved do not stretch [36]. Ghafari et al. demonstrated the use of the electrospinning technique as a self-polarized fabrication method for PVDF nanofibers. This approach achieved a β-phase fraction of 75% in the electrospun PVDF, representing a 41% increase compared to the β-phase content in spin-coated samples. The prepared sensors of electrospun PVDF were most efficient within the 1 kHz–100 kHz frequency range, while its detection capability significantly declines at frequencies below 1 kHz and above 100 kHz [37]. Fortunato et al. demonstrated that the DC magnetic poling of $CoFe_2O_4$-enhanced PVDF–TrFE composite films effectively increased the piezoelectric coefficient d_{33}, achieving values up to 39 pm/V, offering a promising alternative to conventional poling techniques [38].

The literature extensively covers polarization treatments and their impacts on PVDF films, yet there is comparatively less discussion regarding the polarization process for electrospun PVDF fibers due to the structural limitation of nanofibers. Therefore, further research is needed to explore and optimize the electric polarization process of PVDF nanofibers to unlock their full potential for self-powered force sensor applications. Combining processing techniques such as directional stretching, annealing at specific temperatures, and controlled electrical poling can greatly enhance the sensitivity of PVDF for sensors. In this work, statistical optimization by a Design of Experiments (DoE) is performed to systematically explore the influence of multiple variables (such as stretch ratio, heat treatment temperature, electric field, and polling time) on the polarization process, predict the effectiveness level of these factors and identify the optimal conditions for maximizing desired properties, such as the β-phase and piezoelectric sensitivity of PVDF nanofibers for sensor application. For this investigation, a specially designed experimental setup was utilized, enabling a maintained temperature, stretching, and the application of an external electric field to the fiber mats. For the heat treatment of PVDF, the maximum temperature selected was 120 °C, considering that the melting point of the PVDF grade used is 138 °C. The electric field was maintained at a sufficiently low level to prevent any damage to the polymer chains. The levels of % stretch were determined with the aim of preventing plastic deformation in the materials. The analysis was performed by measuring the % F(β), the dielectric properties, the voltage generation capability of electrically polarized

PVDF nanofiber mats, the piezoelectric voltage coefficient (g_{33}), and the piezoelectric charge coefficient (d_{33}) under a low level of force and very low frequency (less than 2 Hz). This polarized PVDF nanofiber mat could be used in low-frequency force-sensing devices due to its enhanced piezoelectric properties, making it ideal for detecting mechanical stimuli. Self-powered piezoelectric sensors can be employed in versatile applications such as touch-sensitive screens, robotic force measurement, smart object recognition, and human health monitoring, including pulse detection, respiratory tracking, and gait analysis, offering sustainable solutions for wearable devices.

2. Materials and Methodology

2.1. Materials

Kynar 740 PVDF with molecular weight of 280,000 g/mol was purchased from Arkema group, Burlington, ON, Canada. N,N-Dimethylformamide (DMF), with a molecular weight of 73.09 g/mol and a purity of 99.8%, was sourced from ACP Chemicals, Montreal, Canada and used to prepare the PVDF solution for electrospinning.

2.2. Methodology

The F(β) of PVDF is influenced by the electrospinning parameters, as the adjustment of the optimal parameters results in increased chain stretching and improved crystallinity, facilitating the formation of β-phase crystals. In an earlier study [35], careful adjustment of the electrospinning parameters was undertaken to optimize key response variables, including maximizing F(β), reducing the fiber diameter, enhancing the alignment of the fibers, and enhancing fiber uniformity. The electrospun mat of PVDF was prepared by following the already optimized process parameters outlined in Table 1.

Table 1. Process parameters for the electrospinning of the PVDF solution.

Concentration	Voltage	Flowrate	Drum Speed	Needle ID	Collector to Tip Distance
23 wt.%	20 kV	1 mL/h	1200 rpm	0.26 mm	13 cm

A DoE approach was utilized to optimize the polarization parameters using a definitive screening design, which aids in the efficient detection of the main effects of the input parameters leading to a specific outcome. Minitab Statistical Software Version 21.1.0 was used for the experimental design, predictive modeling, and data analysis. This study investigates the effect of different heat treatments, electric field intensities, and stretch ratios on electrospun PVDF mats at different time intervals, as shown in Table 2.

Table 2. Electrical polarization control factors and levels for definitive screening design.

		Unit	Level 1	Level 2	Level 3
Control Factors	Heat Treatment Temperature (under 10% stretch for 30 min)	°C	30	75	120
	Electric field	kV/cm	1.5	2.5	3.5
	Stretch Ratio	%	10	20	30
	Time	min	20	50	80

Each parameter was subjected to three levels of variation. The complete step-by-step process is demonstrated by the flow diagram in Figure 1. The design consists of 13 rows that require experimental trials.

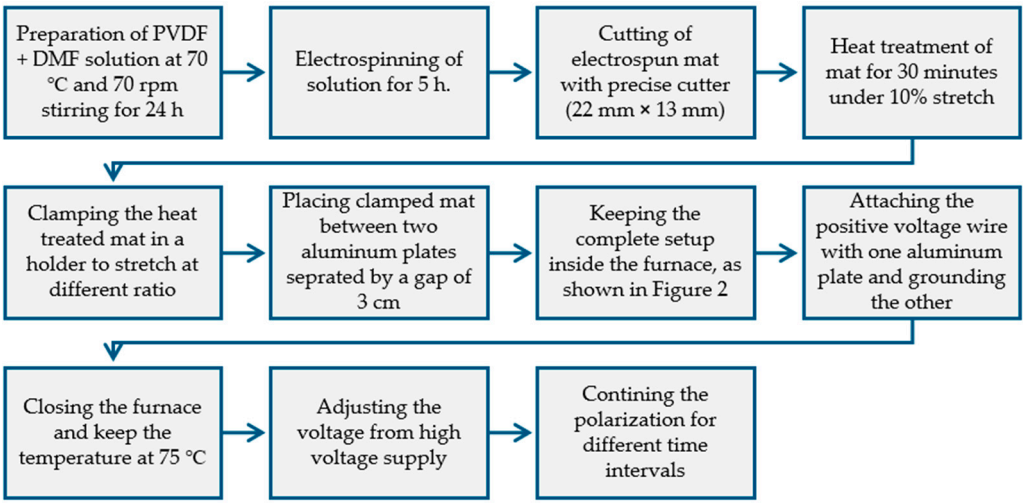

Figure 1. Step-by-step process for the electrospinning and electrical polarization of PVDF.

For the electrical polarization of PVDF, the electrospun mat was heat treated (at varied temperatures between 30–120 °C) in a Dynamic Mechanical analyzer (DMA) while under stretch (10%) for 30 min. DMA Q800 by TA Instruments (New Castle, DE, USA) was used for heat treatment of samples while stretched because of the instrument's high precision in stretching and temperature. After heat treatment, the mat was stretched (varied from 10% to 30%) and placed between two aluminum plates for varied times (20–80 min) and electric field intensity (1.5 kV/cm to 3.5 kV/cm). During the electrical polarization process, the stretched mat along with electrode plates was placed in a furnace, and the temperature was maintained at 75 °C. The electrical polarization setup was constructed as shown in Figure 2.

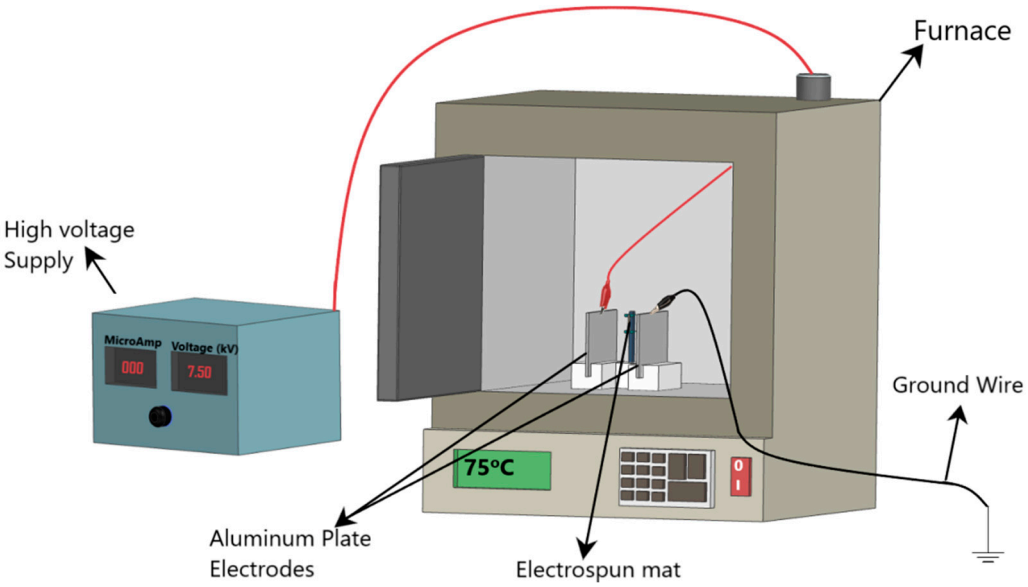

Figure 2. Electrical polarization setup for PVDF electrospun mat.

2.3. Characterization

The morphology of the electrospun PVDF nanofiber mat was analyzed using a Hitachi FlexSEM 1000 Scanning Electron Microscope (SEM) (High Technologies America,

Clarksburg, MD, USA). The characterization techniques employed to assess the F(β) were Perkin Elmer Fourier Transform Infrared Spectroscopy (FTIR) (Waltham, MA, USA) and Bruker X-ray diffractometry (Billerica, MA, USA). Digital Microscope—Keyence VHX-1000 (Osaka, Japan) was used for measuring the thickness of the prepared electrospun mat. The RIGOL Digital Oscilloscope MSO1000Z/DS1000Z (Beijing, China) was used for measuring the voltage produced by applying different levels of stress at different frequencies. The WAGNER FDIX FTK100 (Greenwich, CN, USA) force gauge was used for applying precise force on the sensor. The impedance and dielectric properties of the samples were obtained under 1 N force by Metrohm Autolab PGSTAT204 (Herisau, Switzerland) integrated with the booster BSTR10A.PG204.S (Herisau, Switzerland).

3. Results and Discussion

3.1. Morphology and Porosity Analysis

Figure 3 shows the SEM image of the electrospun nanofibers fabricated by the electrospinning process. The fiber diameter was analyzed using ImageJ software version 1.54g, where measurements were performed on 100 individual fibers randomly selected across various regions of the nanofiber mat. A histogram was subsequently generated to assess the distribution and uniformity of the fiber diameters, providing insight into the morphological consistency of the electrospun structure.

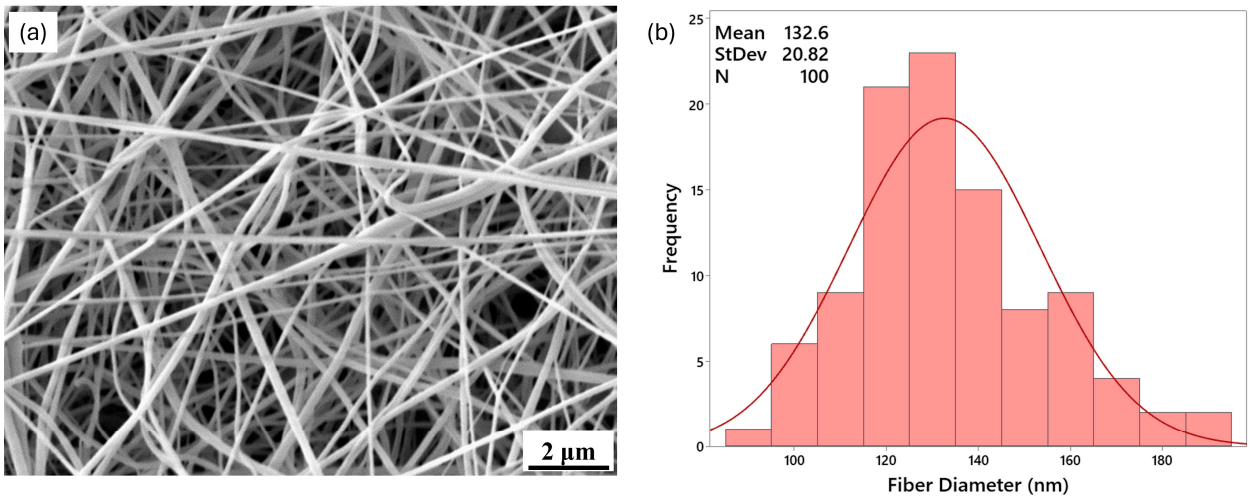

Figure 3. (**a**) Scanning electron microscopy (SEM) image of electrospun PVDF; (**b**) fiber diameter distribution.

In electrospinning, a reduced fiber diameter, along with good uniformity in the fiber diameter, improves the mechanical properties. In addition, minimal defects and bead-free fibers can improve the mechanical properties and significantly enhance the voltage output under an applied force, thereby increasing the material's sensitivity [39,40]. The mean fiber diameter obtained was 132.6 nm.

It was observed that the porosity of the structure is closely linked to the piezoelectric properties of the material. To calculate the porosity, digital image processing was performed on the SEM high-resolution image. As can be seen in Figure 3, there are pores and solid structures in the electrospun scaffold. MATLAB was used for image processing, by undertaking the following steps:

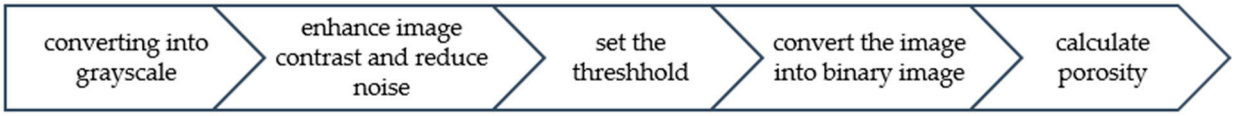

Figure 4 shows the binary image obtained at three different threshold values following the literature [41]; thresholds were determined as functions of the mean (μ) and standard deviation (σ) of the pixel values in the image. For surface layers, the threshold was set to (μ + σ) to capture higher-intensity features, eliminating the lower layers and isolating only the surface layers. For the surface and intermediate layers, the threshold was defined as μ to focus on the average pixel intensity, capturing a combination of both the surface and middle layers. For all layers combined, the threshold was established at (μ − σ) to detect lower-intensity features, allowing for a balanced assessment of porosity across different image regions. The calculated digital porosity (DP), shown in Figure 4, demonstrated that the image threshold significantly influences the observed nanofiber layers. By adjusting the threshold, different layers of nanofibers can be identified. Overall, threshold 2 (μ) gives a DP of 49% more reliably than threshold 1, which considers a lot of lower-layer fibers as pores while threshold 3 does not count the pores from upper-fiber layers. However, the % porosity was further verified in the dielectric testing section.

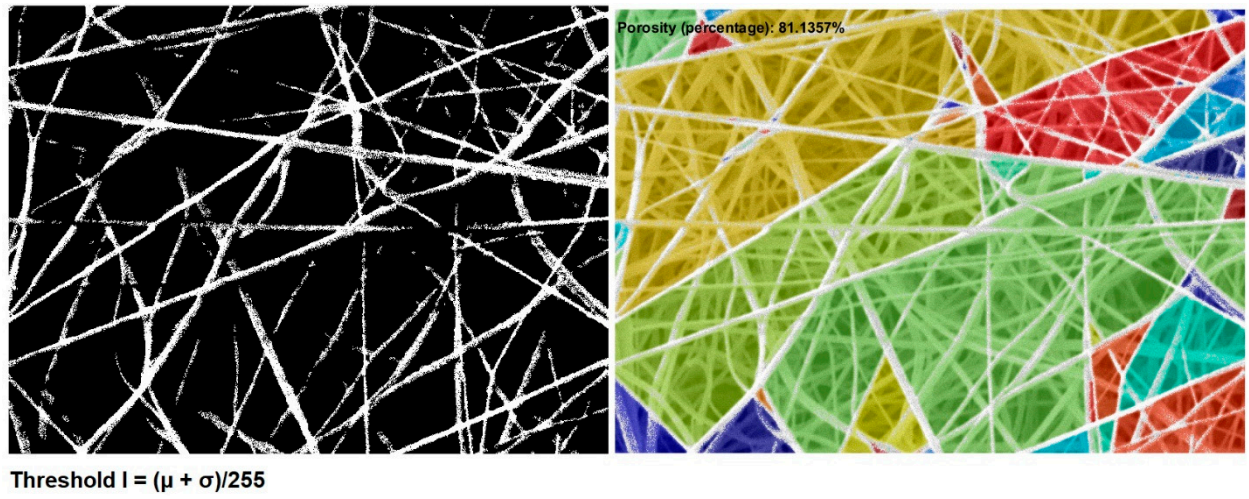

(**a**)

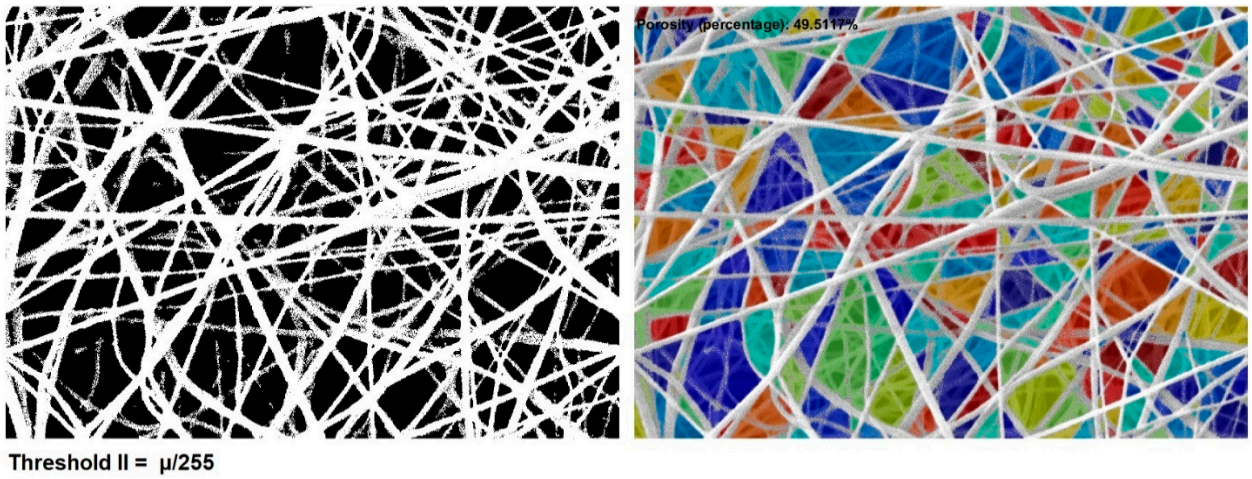

(**b**)

Figure 4. *Cont.*

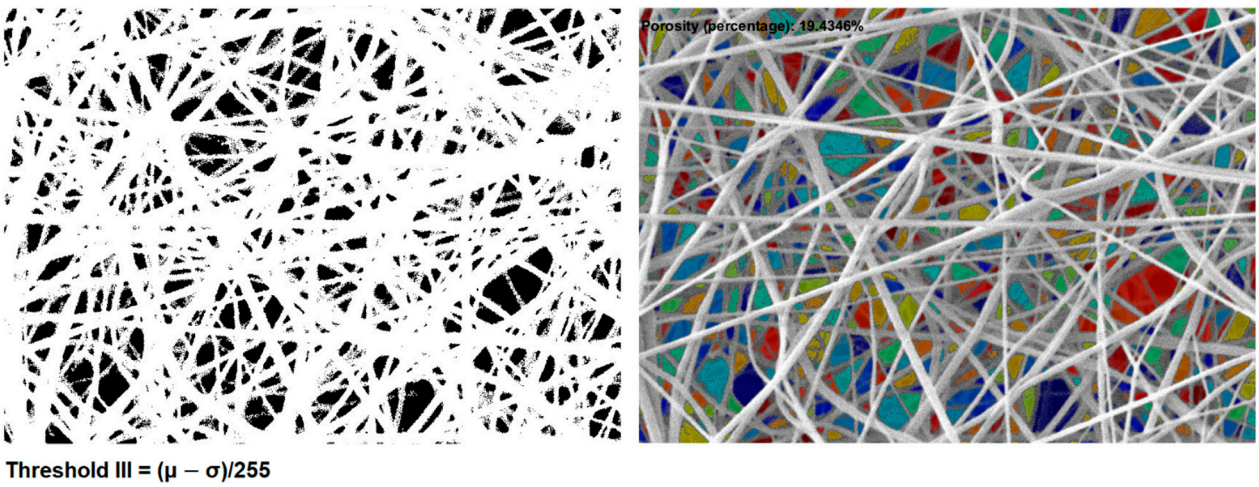

(**c**)

Figure 4. Processed micrographs of electrospun PVDF at three different thresholds (**a**) Threshold I, (**b**) Threshold II, (**c**) Threshold III.

3.2. β-Phase Fraction

FTIR spectroscopy was used as a primary tool for interpreting the vibrational motions associated with the chemical bonds within the molecular structure of PVDF across different polymorphs. Additionally, the FTIR spectra enabled the quantification of the F(β) within the polarized PVDF nanofiber mat. Figure 5 shows a comparison of PVDF electrospun mats with no polarization treatment and polarized mats, each exhibiting varying % (F(β)) values, as depicted in their respective FTIR spectra. Peaks corresponding to distinct chemical bonds within PVDF are mentioned, including the vibrational bands of the α-phase observed at 760 cm^{-1} (CF_2 bending and skeletal bending), and the β-phase bands at 840 cm^{-1} (C-F_2 asymmetric stretching and CH_2 rocking), and 1280 cm^{-1} (CF out-of-plane deformation). A more detailed explanation of each peak is given in Table 3. The influence of the polarization process parameters on the F(β) of PVDF was obtained from the FTIR spectra using Equation (1) [35,42].

$$F(\beta) = \frac{X_\beta}{X_\alpha + X_\beta} = \frac{A_\beta}{(K_\beta/K_\alpha)A_\alpha + A_\beta} = \frac{A_\beta}{1.3A_\alpha + A_\beta} \quad (1)$$

where

A_α = absorbances at 760 cm^{-1} (refer to the α-phase of PVDF)

A_β = absorbances at 840 cm^{-1} (refer to the β-phase of PVDF)

K_β and K_α are reported as absorbance coefficients of 7.73 × 104 and 6.13 × 104 cm^2/mol, respectively [42,43].

Figure 5 illustrates that the polarized electrospun mat EP-5 (processed under the conditions of 120 °C heat treatment, an electric field of 3.5 kV/cm, 20% stretch, and 80 min duration) exhibits a minimal band associated with the α-phase and a pronounced presence of the β-phase. The measured % F(β) of EP-5 is 95%. EP-3 (processed under the conditions of 30 °C heat treatment, an electric field of 2.5 kV/cm, 10% stretch, and 80 min duration) exhibited a β-phase fraction of 85%, with a relatively weak α-phase peak. In contrast, the non-polarized PVDF electrospun mat (P) displayed a significantly intense peak associated with the α-phase compared to the other two polarized PVDF mats, and the measured β-phase was 75%.

To validate the findings of FTIR, XRD analysis was conducted to identify and quantify the percentage of % F(β). A cobalt source was used for X-ray generation, yielding high-

quality diffractograms and enabling clear phase identification. Most research reports the use of a copper source for the XRD analysis of PVDF. To ensure comparability with existing studies, the 2θ values were converted using TOPAS software (version 6) [35]. A comparison of the XRD pattern of three electrospun mats is exhibited in Figure 6. In the XRD pattern of α-PVDF, diffraction peaks are observed at 21.35° and 30.5°, corresponding to the (020) and (021) reflections, respectively. On the other hand, the XRD pattern of β-phase PVDF exhibits characteristic peaks at 23.9°, 42.19°, and 48.14°, which correspond to (110)/(200), (101), and (111) diffracting planes [35]. To calculate the β-phase, Equation (2) was used [42].

$$F(\beta) = \frac{I_\beta}{I_\alpha + I_\gamma + I_\beta} = \frac{I_{(110/200)} + I_{(101)} + I_{(111)}}{I_{020} + I_{(110/200)} + I_{021} + I_{002} + I_{(101)} + I_{(111)}} \quad (2)$$

where I_α, I_γ, and I_β denote the peak intensity for the α, γ, and β-phases, respectively [42,44,45]. EP-8 (processed under the conditions of 120 °C heat treatment, an electric field of 2.5 kV/cm, 10% stretch, and 80 min duration), with 93% β-phase, displayed a very intense peak at 23.9°, which is associated with the β-phase. EP-4 (processed under the conditions of 120 °C heat treatment, an electric field of 1.5 kV/cm, 30% stretch, and 20 min) clearly shows a less intense β-phase peak than to EP-8. The measured β-phase of EP-4 in FTIR as well as in XRD was 89%. The least intense peak of the β-phase can be seen in the non-polarized electrospun mat of PVDF (P).

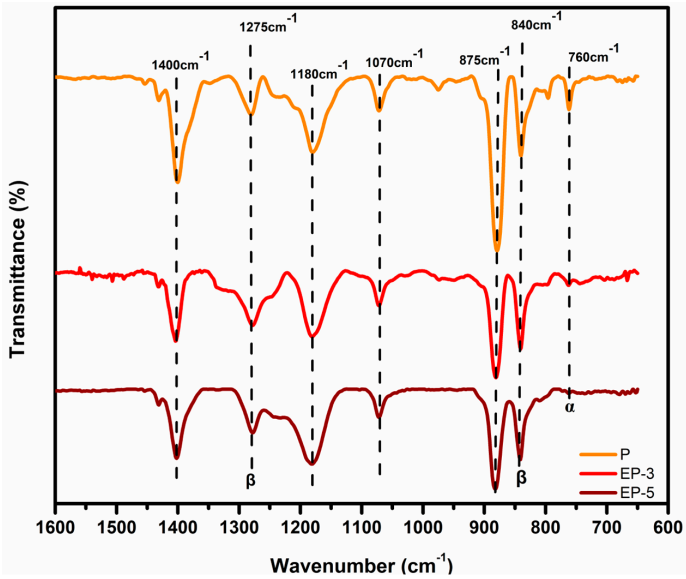

Figure 5. FTIR spectra of PVDF nanofibers, nonpolarized (P), and polarized mat (EP-3 and EP-5).

Table 3. Detailed explanation of FTIR spectra peaks in PVDF.

Frequency	Assignment
1400 cm^{-1}	C-H bending associated with methylene in aliphatic
1280 cm^{-1}	C-F_2 out-of-plane deformation due to the β-phase,
1180 cm^{-1}	C-H rocking motion
1070 cm^{-1}	Vibration due to C-H in-plane and out-of-plane deformation
875 cm^{-1}	Amorphous PVDF
840 cm^{-1}	C-H_2 rocking in the β-phase and C-F_2 asymmetric stretching due to β-phase
760 cm^{-1}	C-F_2 due to the α-phase

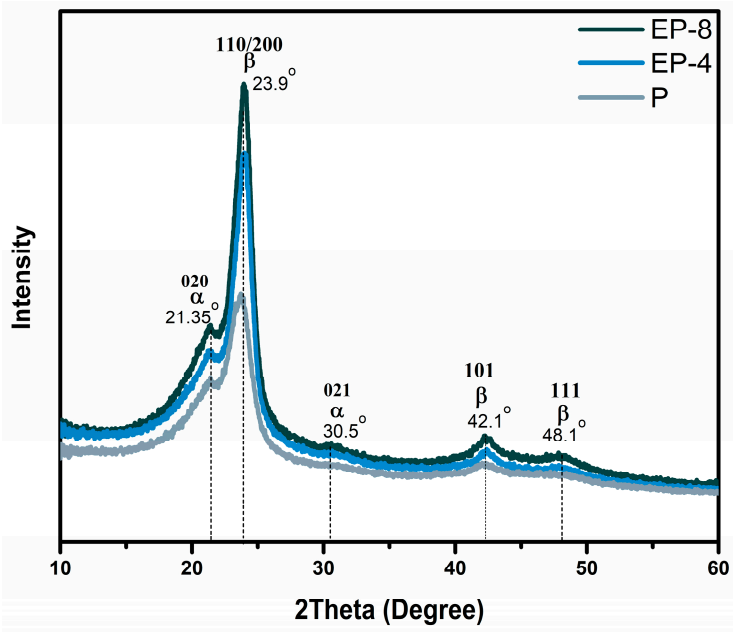

Figure 6. Comparison of XRD pattern of nonpolarized (P) and polarized PVDF electrospun mats (EP-8, EP-4).

The application of thermal treatment to electrospun PVDF nanofibrous films promotes the formation of the β phase and enhances the crystalline structure. Under these conditions, the nanofibrous film treated at 120 °C exhibits a high polar β-phase that is clear from the FTIR spectra and XRD pattern of EP-4, EP-5, and EP-8. Annealing the nanofiber mat at higher temperatures was favorable for the conversion of non-polar α-phase into polar β-phase through the rearrangement of the molecular chain orientation, which is visible from a significant reduction in the α-phase peak in FTIR [46,47].

The electric field also contributes to the enhancement of F(β), as can be observed from the graphs comparing the XRD pattern and FTIR spectra. When a high electric field is applied, torque is exerted on the dipole moments in the polymer chains, causing the chains to rotate. This rotation aligns the dipoles along the direction of the electric field, increasing the F(β) and enhancing the piezoelectric response [48].

It was observed that the longer the duration of polarization, the more pronounced the effects on the β-phase. Extended polarization times can promote the growth of crystalline regions within the polymer, particularly in the β-phase. Both EP-5 and EP-8 were polarized for 80 min, resulting in very high β-phase contents of 95% and 93%, respectively.

Figure 7 illustrates the factorial main effects of the electrical polarization parameters on the β-phase of the PVDF nanofiber mat obtained from definitive screen design analysis.

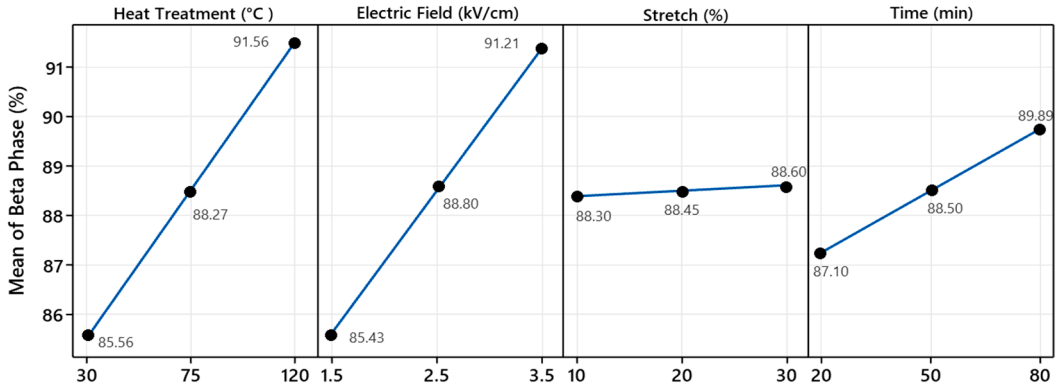

Figure 7. The main effect plots obtained from the definitive screen design analysis for the β-phase.

The parameter with the greatest influence on the β-phase was observed to be the heat treatment, which ranged from 30 °C to 120 °C, and the electric field, which ranged from 1.5 kV/cm to 3.5 kV/cm. Conversely, % stretch was noted as the least influential factor because a substantial amount of stretching was performed during the electrospinning process. A mathematical model was developed using fit regression analysis in Minitab software to predict the values of response variable % F(β). The regression equation, which demonstrates the relationships between process factors for the output response variable, is presented here:

$$Y = \varepsilon + 0.0666 \times Heat\ Treatement + 2.889 \times Electric\ field + 0.011 \times Stretch\% + 0.0416 \times Time \quad (3)$$

Y = response (% β-phase).

ε = 73.97 is the error normally distributed on output response Y.

A comparison between the experimental results and the mathematical model is visually illustrated in Figure 8, facilitating an evaluation of the model's accuracy.

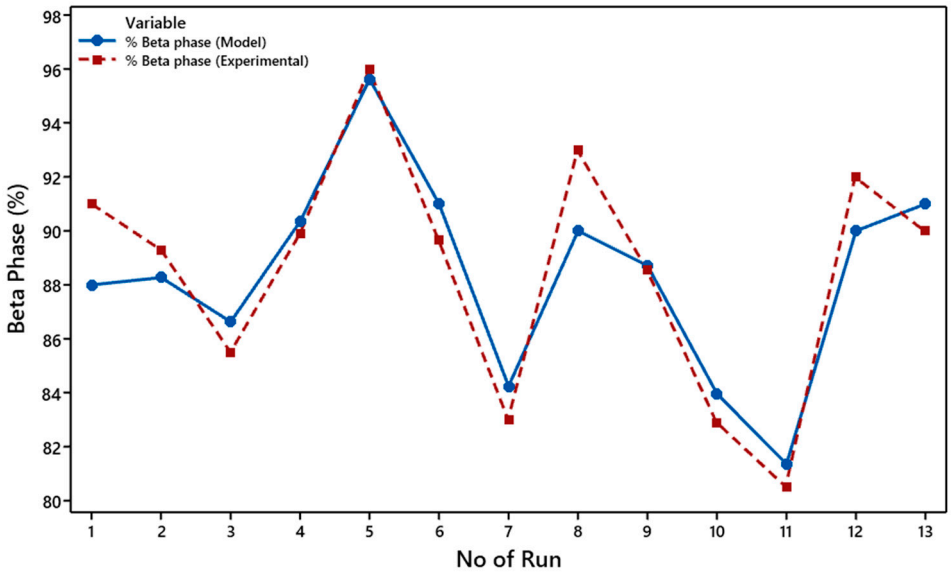

Figure 8. Mathematical model validation of the % β-phase content with experimental results.

The model provided a coefficient of determination (R^2) of 73% for the full experimental runs at a 95% confidence interval. This indicates that 73% of the variability in the independent factors is explained by the model. Model terms with *p*-values below 0.05 are considered significant. This model showed high accuracy for heat treatment (*p*-value = 0.013) and voltage (*p*-value = 0.016). However, it was a poor fit for time and % stretch, as their *p*-values were greater than 0.05. To improve the model's accuracy, one could either increase the number of experimental runs or incorporate the interaction effect model. The lowest % F(β) value, 81%, was recorded for EP-11 processed with a 30 °C heat treatment, an electric field of 1.5 kV/cm, and a 20% stretch for 20 min.

The % F(β), as a function of the applied electric field and heat treatment temperature during the polarization process, is displayed in Figure 9a. The combined effect of two factors on the response variable % F(β) was analyzed by keeping the % stretch and time constant at 20% and 80 min, respectively. It was found that at the highest temperature (120 °C) and maximum applied electric field (3.5 kV/cm), the % F(β) is 95%. At 120 °C, the minimum % F(β) (in the range of 87.5–90%) was at the lowest electric field applied (1.5 kV/cm). At the lowest heat treatment temperature of 30 °C, the maximum % F(β) observed was also in the range of 87.5–90%. At an electric field higher than 2.5 kV/cm

and temperature greater than 80 °C, the % F(β) is higher than 90%. Figure 9b illustrates the combined influence of time and the heat treatment temperature on % F(β) while maintaining the electric field at 3.5 kV/cm and % stretch at 20. Regardless of the time taken for electrical polarization, the % F(β) exceeds 93% at a temperature of 120 °C. A polarization time exceeding 50 min and a heat treatment temperature exceeding 75 °C result in a % F(β) higher than 90%. Figure 9c exhibits the effect of time and electric field on the % F(β) when keeping the % stretch and heat temperature at 20% and 80 °C, respectively. When the electric field is lower than 2.5 kV/cm, even when the maximum polarization time is used, the % F(β) is always less than 90%.

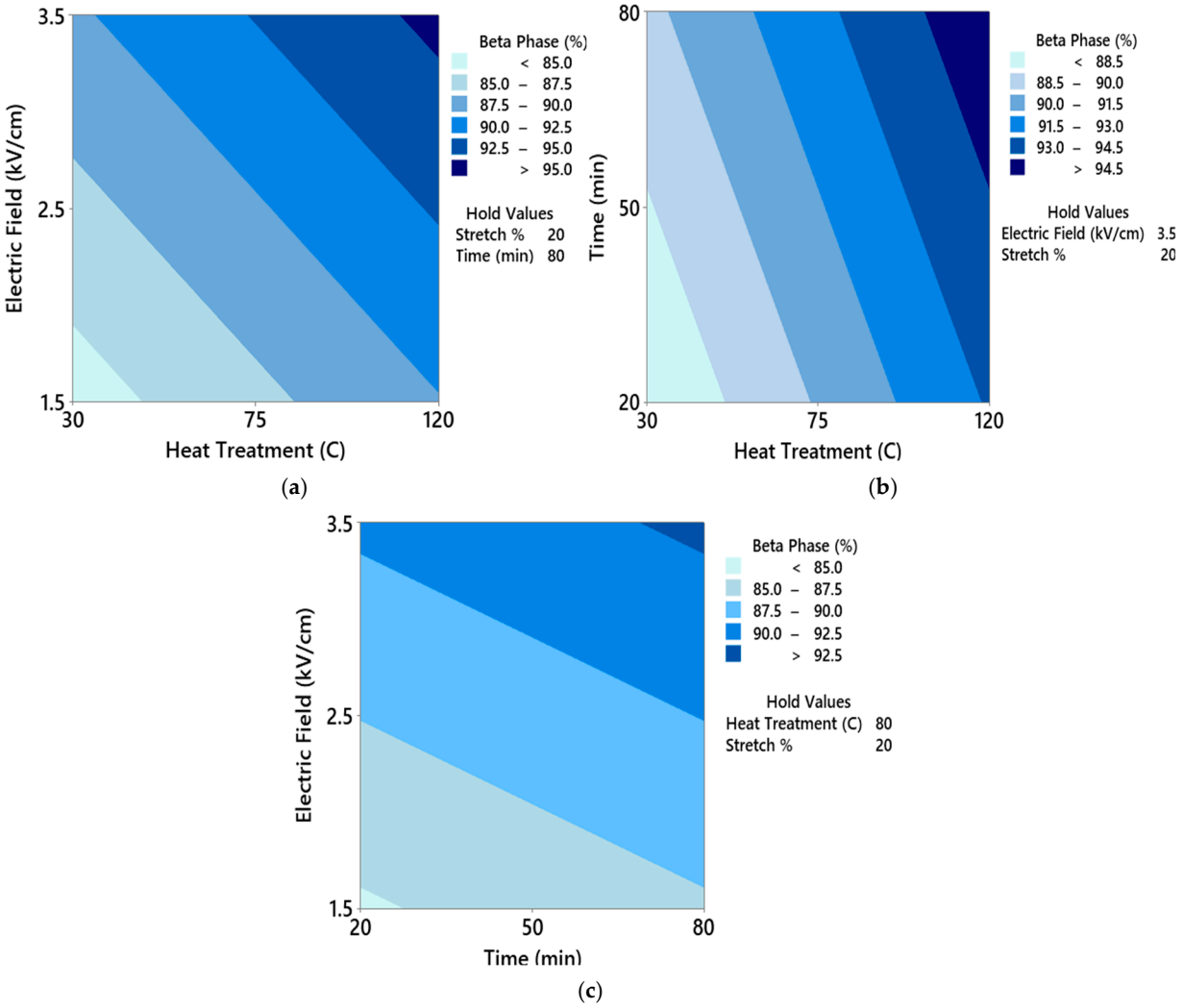

Figure 9. Contour plot of % of β-phase as a function of (**a**) heat treatment and electric field; (**b**) heat treatment and time; and (**c**) electric field and time.

3.3. Impedance and Dielectric Properties

Electrochemical Impedance Spectroscopy (EIS) analysis was carried out on the electrospun film at a constant potential of 0.35 V, with the frequency ranging from 1 Hz to 1 MHz. The impedance and capacitance data were obtained over the set frequency range by placing the round-shaped thin films (diameter was 12 mm) between two electrodes. The dielectric constant of the samples was calculated using Equation (4) [49,50].

$$\varepsilon' = \frac{C \times d}{\varepsilon_o \times A} \quad (4)$$

where C is the capacitance (F), d stands for the distance between the electrodes or thickness of the film (m), ε_o is the vacuum permittivity (8.85×10^{-12} Fm^{-1}) and A is the electrode area (m^2).

Figure 10 shows the Nyquist plots obtained for the non-polarized PVDF electrospun mat (P) and polarized electrospun mat (EP-5, EP-4, EP-11). It can be observed that despite the fibrous structure of the material, it displays high homogeneity and less deviation from the semicircle. This shows that the material has good charge transfer and that the EIS results are reliable. A few irregularities were observed; these were possibly due to the lesser contact of the electrode with the fibrous structure [51]. The real (Z') and imaginary part (Z'') of the impedance were used to calculate the dielectric loss ($\mathcal{E}''$) of the films by following Equation (5) [52].

$$\varepsilon'' = \frac{Z'}{\omega \times C \left(Z''^2 + Z'^2\right)} \quad (5)$$

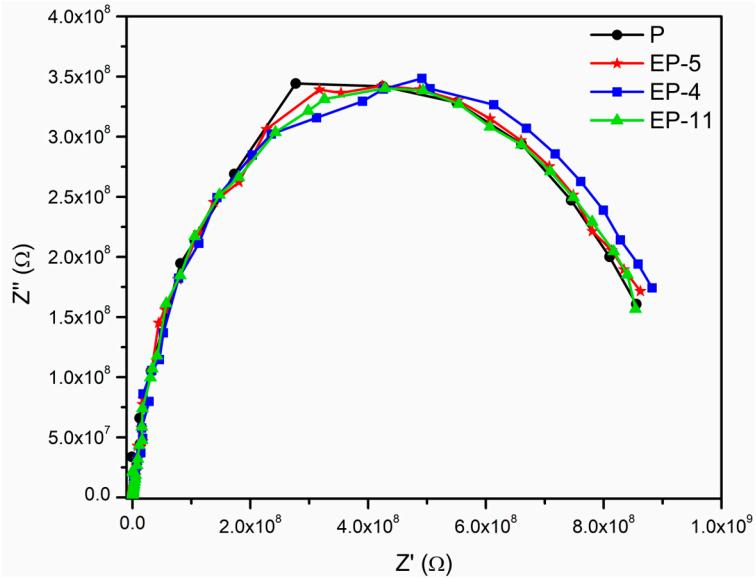

Figure 10. Nyquist plots for polarized and non-polarized electrospun PVDF.

Figure 11 displays the (a) dielectric constant ($\mathcal{E}'$) and (b) dielectric loss ($\mathcal{E}''$) vs. frequency for the polarized and non-polarized electrospun mats. Overall, with an increase in frequency, there is a decrease in the value of $\mathcal{E}'$, which is a very typical trend. At lower frequencies, the decrease in the $\mathcal{E}'$ is very sharp compared to that at higher frequencies. The $\mathcal{E}'$ of a material is typically influenced by four primary types of phenomenon: ionic, electronic, orientational, and space charge polarization. At low frequencies, all these mechanisms can contribute to the overall $\mathcal{E}'$. As the frequency increases, due to the rapidly changing electric field, the dipoles struggle to keep pace, which leads to a change in the $\mathcal{E}'$. When the electric field has a higher frequency, the alternating direction of the field accelerates, requiring the more rapid switching of dipoles. This switching requires time, and as the frequency increases, the available time for dipole alignment decreases, eventually causing the dipoles to lag behind the field. When a critical frequency is reached, the dipoles become unable to align with the electric field, resulting in a lack of polarization within the film and diminishing its dielectric behavior [52,53]. With the increase in the frequency, the contribution from the space charge, ionic, and orientational polarization reduces, leaving electronic polarization as the primary contributor to the $\mathcal{E}'$. PVDF is a polar polymer and β-phase PVDF has a higher density of dipoles. A greater alignment of dipoles corresponds to a higher $\mathcal{E}'$. The most dominant type of polarization that occurs in PVDF is orientational

polarization. In Figure 11a, non-polarized PVDF (P), with a β-phase of 75%, and EP-11, with a β-phase of 81%, exhibit almost the same value (25 at 1 Hz) and trend for $\mathcal{E}'$. However, EP-5, with a β-phase of 95%, and EP-4, with a β-phase of 90%, have a high $\mathcal{E}'$ (almost 30 at 1 Hz). From 1 Hz to 1 MHz, the polarized PVDF with a high β-phase (higher than 85%) shows a greater value for $\mathcal{E}'$.

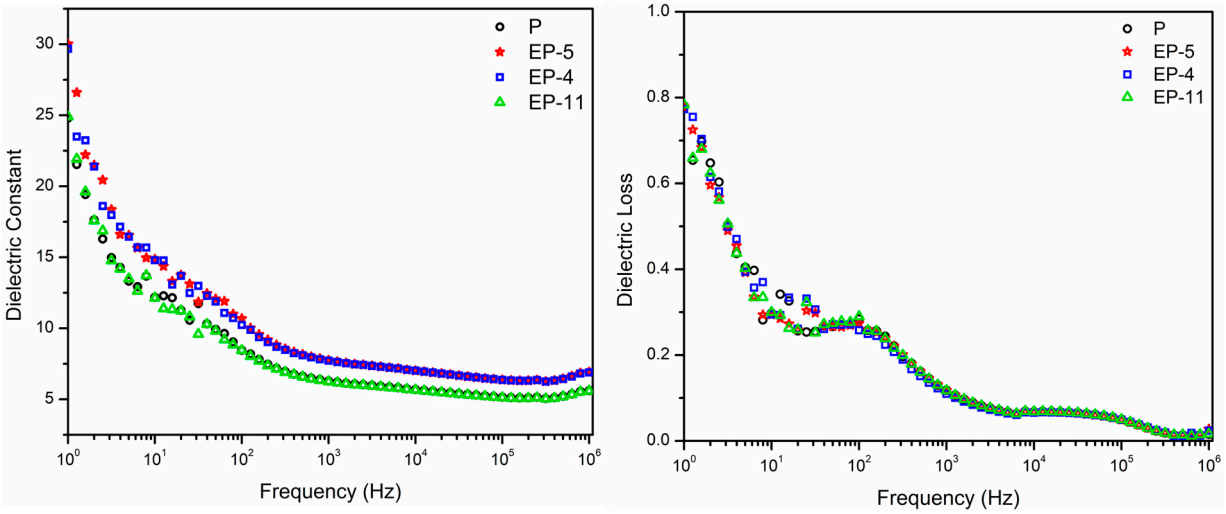

(**a**) (**b**)

Figure 11. (**a**) Dielectric constant ($\mathcal{E}'$) and (**b**) dielectric loss ($\mathcal{E}''$) of polarized and non-polarized electrospun PVDF.

$\mathcal{E}''$ refers to the process in which energy is consumed and heat is generated as a material undergoes polarization in response to an electric field [54,55]. At lower frequencies, $\mathcal{E}''$ is high because different types of polarization happen at the same time. However, at higher frequencies, dipoles do not have enough time to realign with the field, so less energy is lost. Therefore, only electronic polarization can respond, which reduces the amount of energy lost, leading to a lower $\mathcal{E}''$ [56]. At a frequency higher than 104, the change in $\mathcal{E}''$ is much lower, which shows that αc-relaxation is occurring. αc-relaxation occurs in crystalline polymers due to the presence of imperfections in crystalline regions, such as crystal defects, chain loops on lamellar surfaces, and chain rotation between the crystalline and amorphous regions [52]. It was noted that all electrospun PVDF samples were either polarized or non-polarized, with different % F(β) values showing a similar $\mathcal{E}''$.

Generally, the $\mathcal{E}'$ of PVDF film in the literature is between 10 and 12 at 1 kHz [52]. In this work, electrospun PVDF showed a value between 6.2 and 7.6 for all samples at 1 kHz. The lower value of $\mathcal{E}'$ is due to the presence of air in the pores [48]. To relate the measured DP with the measured $\mathcal{E}'$, the simplified Bruggeman Effective Medium Approximation (EMA) model was used because of its high effectiveness. Bruggeman EMA was applied according to Equation (6) [57,58], and the theoretical $\mathcal{E}'$ was calculated at different porosity values.

$$f_f \frac{\varepsilon_f(\omega) - \varepsilon_{eff}(\omega)}{\varepsilon_f(\omega) + 2\varepsilon_{eff}(\omega)} + f_{air} \frac{\varepsilon_{air}(\omega) - \varepsilon_{eff}(\omega)}{\varepsilon_{air}(\omega) + 2\varepsilon_{eff}(\omega)} = 0 \quad (6)$$

where ε_f is the dielectric constant of fibers, ε_{air} is the dielectric constant of air, ε_{eff} is the effective dielectric constant, f_f is the volume fraction of fibers and f_{air} is the volume fraction of air.

A comparison of the theoretical $\mathcal{E}'$ at different porosity values with the measured $\mathcal{E}'$ is presented in Figure 12.

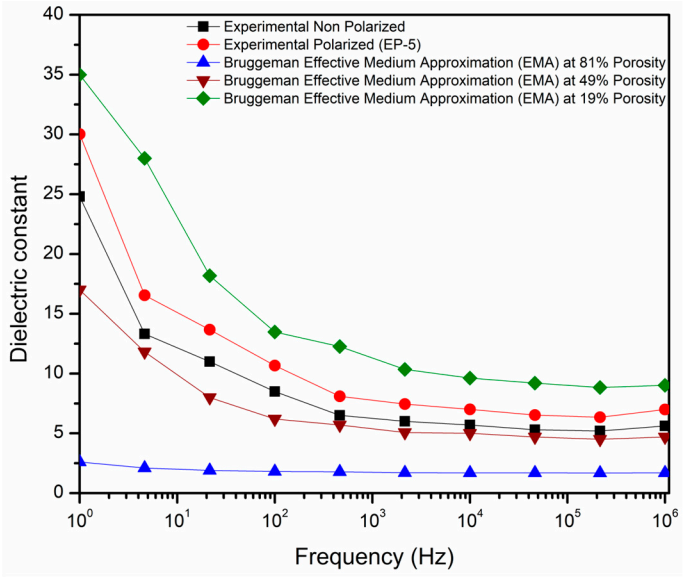

Figure 12. Comparison of the measured dielectric constant ($\mathcal{E}'$) with the calculated $\mathcal{E}'$ at different digital porosities (DPs) % using Bruggeman Effective Medium Approximation.

From the plot, it can be seen that the Bruggeman EMA, when applied with 49% porosity, showed an $\mathcal{E}'$ that was more similar to the measured value for both the non-polarized and polarized PVDF electrospun mat.

3.4. Piezoelectric Properties

To quantitatively measure the sensitivity of the polarized and non-polarized PVDF electrospun mat, a setup was designed and sensors were made, as shown in Figure 13. The electrospun mat was cut using a precise cutter with dimensions of 15 mm × 13 mm × 0.3 mm. Copper tape was used for the electrodes and applied to both sides of the mat. The central area containing the mat and electrodes was then encapsulated in plastic film tape, as illustrated in Figure 13. The measured thickness of the mat obtained from the digital microscope was in the range of 0.2–0.3 mm. The force gauge was attached to a linear rail guide controlled through Arduino. The linear rail guide was programmed to move up and down at a specific frequency to apply a specific force.

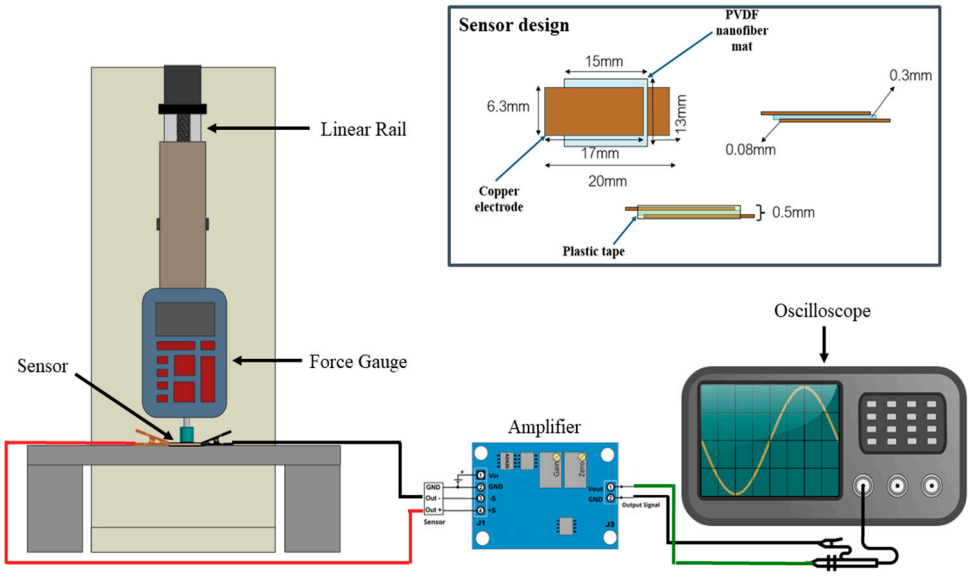

Figure 13. Sensor's sensitivity measurement setup at precise force and frequency.

For the measurement of the voltage signal, the amplifier (AD620) module was connected to the sensor and oscilloscope. This study aimed to produce a soft piezoelectric sensor with a high signal-to-noise ratio (SNR) at a very low level of force and frequency. The amplification factor used was 10 for testing all sensors at three force levels (1 N, 5 N, 10 N) and three frequency variations (0.5 Hz, 1 Hz, 2 Hz). The relationship between the output response of the signal generator and the force applied to the sensor was recorded on an oscilloscope. To analyze or interpret the signal generated by the material in its original form, the amplification factor was removed from the signal before analysis. Each sensor was tested five times, and each time the probe hit the sensor surface five times. It is well known that the triboelectric effect can sometimes be mistaken for piezoelectricity, as both involve the generation of electrical charges. Triboelectricity arises from contact between two dissimilar materials, leading to opposing charges on each surface—a phenomenon known as contact electrification (CE). In piezoelectric materials, CE can occur due to friction at polymer interfaces, shear forces in sensor components, or even static discharge or friction from the contact probe used during sensor testing. If CE is not accounted for, the electrical output attributed to the piezoelectric effect may be inaccurately inflated. To minimize the potential for triboelectric contributions, the piezoelectric element was encapsulated in PET tape as stated above, ensuring that all components remained securely in place and did not slide against one another, thereby eliminating friction or separation between surfaces. Additionally, the contact probe used during testing was designed to apply force without lateral motion or sliding over the sensor surface, further reducing the likelihood of triboelectric charge generation. A control test was conducted following the literature [59] to measure the voltage output using inherently non-piezoelectric silicone rubber under conditions identical to those for the piezoelectric sensor. For this test, a 0.5 mm thick silicone rubber film was sandwiched between two electrodes, replicating the method of preparing the PVDF sensor. The silicone rubber assembly, along with the electrodes, was encapsulated in PET tape to ensure consistency with the sensor's construction. A force of 10 N was applied at a frequency of 1 Hz during the test to evaluate any potential voltage output from non-piezoelectric sources.

The voltage output of the highly electrically polarized PVDF sensor EP-5 when varying the load and frequency is shown in Figure 14a. It can be seen that when the force is 1 N at 2 Hz, the average output voltage of the sensor is 311 mV $\pm$ 13 mV. When applying 10 N, the average value of the output voltage is 631 mV $\pm$ 11 mV. When lowering the frequency of the applied force, the generated voltage is also reduced; when applying 1 N at 0.5 Hz, the produced average voltage signal is 300 mV $\pm$ 11 mV and its maximum rises to 506 mV $\pm$ 5 mV when applying a 10 N force. The data between 1 N and 10 N confirmed that the voltage produced by the sensor increases significantly with the increase in external force for all frequency loadings. At high-frequency force loadings, the electrical impedance of the piezoelectric sensor decreases, allowing it to couple with the external circuit and generate a stronger electrical signal for a given mechanical input. At low frequencies, the impedance increases, reducing the efficiency of charge generation. Moreover, with low-frequency force loadings, the material has more time to relax between stress cycles, leading to a lower effective sensitivity and charge leakage. However, when force is applied with high frequencies, the rapid cycling of stress keeps the material in a more "excited" state, enhancing its sensitivity [60].

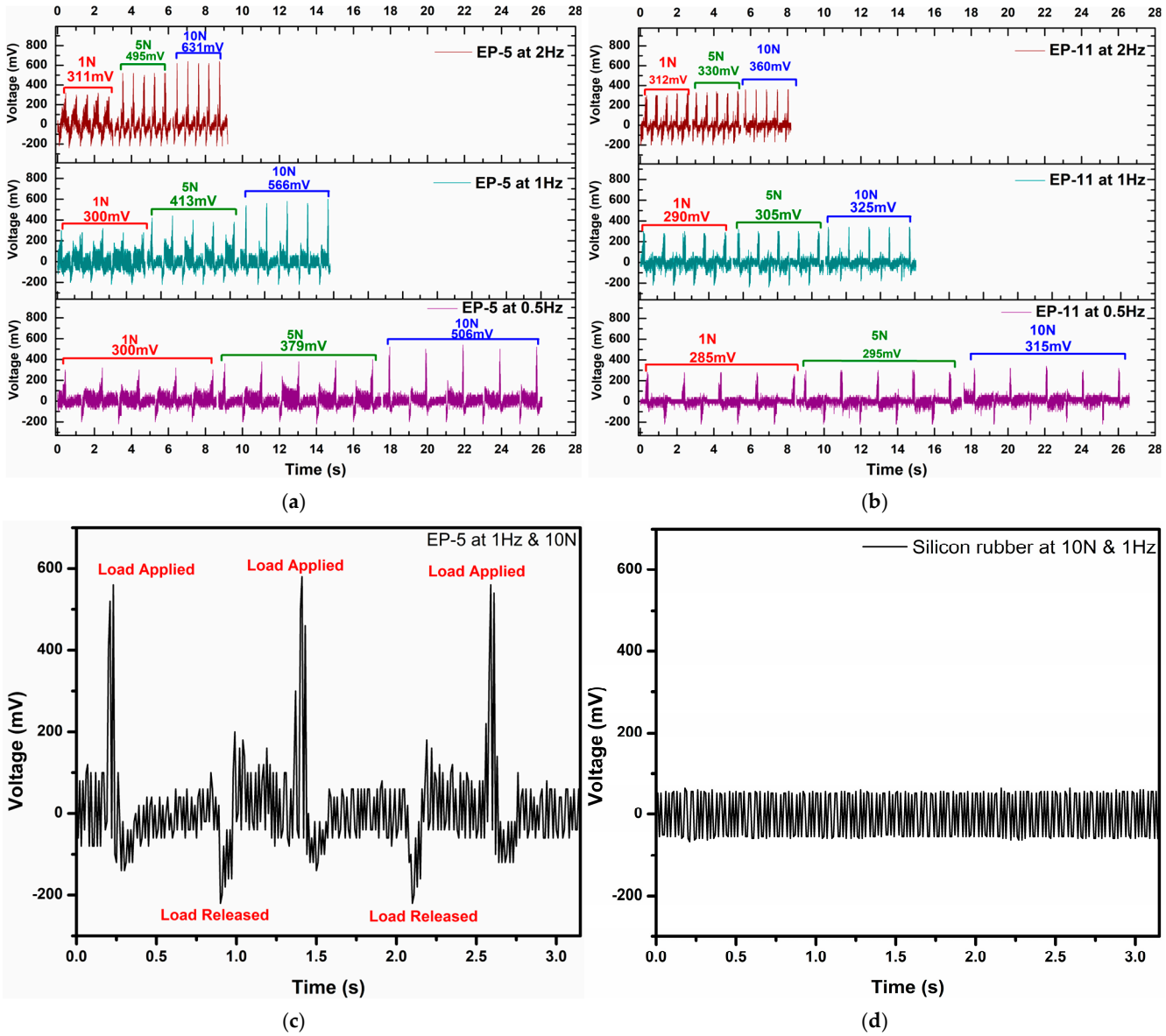

Figure 14. The output response of sensors when applying different force levels at different frequencies: (**a**) high-sensitivity PVDF nanofiber mat (EP-5); (**b**) low-sensitivity PVDF nanofiber mat (EP-11); (**c**) measured response waveform of EP-5 at 1 Hz and 10 N; (**d**) measured response when applying a 10 N force at 1 Hz on silicon rubber.

The voltage output of the least polarized PVDF sensor EP-11 when varying the load and frequency is shown in Figure 14b. The produced voltage was lower than that for EP-5 on each applied force level. It was observed that when applying a 10 N force at 2 Hz, EP-11 produced almost half (360 mV ± 7 mV) of EP-5 at the same force and frequency. Figure 14c displays the waveform of EP-5 when a 10 N load is applied and removed at a 1 Hz frequency. Figure 14d shows the result of the control sample testing performed on silicon rubber. This control test confirmed that no significant voltage output was generated by the non-piezoelectric silicone rubber, ensuring that any observed signals in the piezoelectric sensor testing are indeed attributable to the piezoelectric effect and not triboelectricity.

The sensitivity of a sensing device expressed as $S = \Delta V/\Delta P$ (where ΔV is the relative change in the output voltage of the device, and ΔP is the relative change in the external force) is a critical indicator for assessing its performance. This parameter can be obtained from the slope of the fitting curve. The output of the sensor is linearly fitted by using the data analysis software ORIGIN Pro 2018, and the force–voltage relationship of the

sensor is obtained at each frequency. Figure 15 exhibits the comparison of the sensitivity of EP-5 and EP-11 at different frequencies. It is evident that the sensor's output response linearly increases with the rising amplitude of the exerted force. The high coefficient of determination ($R^2 \geq 99\%$) confirms the linearity of the fit. EP-5 exhibited sensitivities of 35 mV/N, 29 mV/N and 22 mV/N at 2 Hz, 1 Hz and 0.5 Hz, respectively. Meanwhile, EP-11 offered a sensitivities of 5 mV/N, 3.5 mV/N and 3 mV/N at 2 Hz, 1 Hz and 0.5 Hz, respectively.

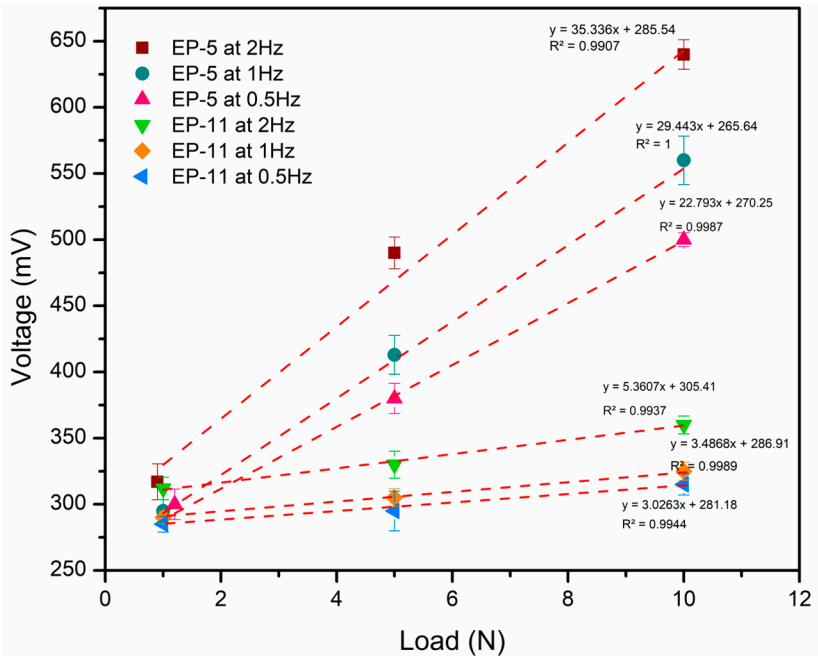

Figure 15. The voltage signal and force relation curve of the high-sensitivity sensor (EP-5) and low-sensitivity sensor EP-11.

The sensitivity data for both polarized and nonpolarized PVDF nanofiber mats is plotted (in Figure 16) against the percentage of β-phase (% F(β)). When the PVDF was originally electrospun, it contained 75% F(β). When electric polarization was performed, the dipoles of the PVDF chains became aligned normally to the surface of the mat film and formed a residual polarization. The residual polarization persisted even in the absence of an external electric field. This enhanced residual polarization enhanced the generated signal when an external force was applied, thereby increasing the sensitivity of the PVDF mat [61]. It was observed that when the β-phase was below 86%, the sensitivity at all tested frequencies was less than 10 mV/N. However, when the β-phase was increased to 90%, the sensitivity of the PVDF material increased from 25% to 35% due to the increased density of the dipoles. This effect was more pronounced at higher frequencies compared to lower frequencies. It was observed that when applying a certain force, the produced signal was repeatable, with a standard deviation of 5–10 mV (for EP-5). This high stability over time is also due to the presence of residual polarization. It helps to maintain a consistent baseline polarization, reducing the drift in the sensor's readings and improving its long-term reliability [61].

To examine the impact of various polarization process factors on PVDF sensitivity across all tested frequencies, a factorial plot was generated using Minitab software to analyze the response variable in the DOE. Figure 17 shows the factorial analysis of the mean sensitivity versus the process variables at three frequencies (2 Hz (Figure 17a), 1 Hz (Figure 17b), 0.5 (Figure 17c)). It was observed that the heat treatment and electric field were significant factors prominently affecting the sensor's sensitivity, similar to in the β-phase.

The polarization time also has a positive impact on the sensor's sensitivity, but the effect is lower compared to the temperature of the heat treatment and electric field. However, an interesting finding was that the percentage of stretch showed a nearly negative trend across all frequencies. Although statistically negligible, the effect was almost zero.

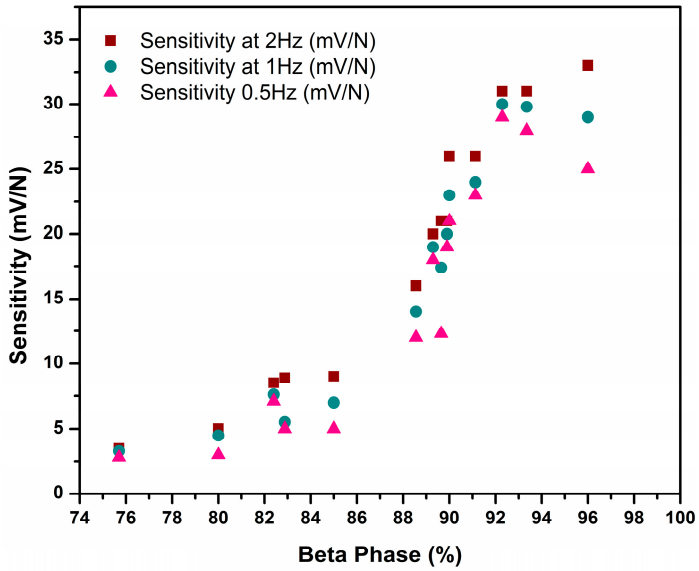

Figure 16. β-phase fraction (% F(β)) versus sensitivity of polarized and non-polarized PVDF.

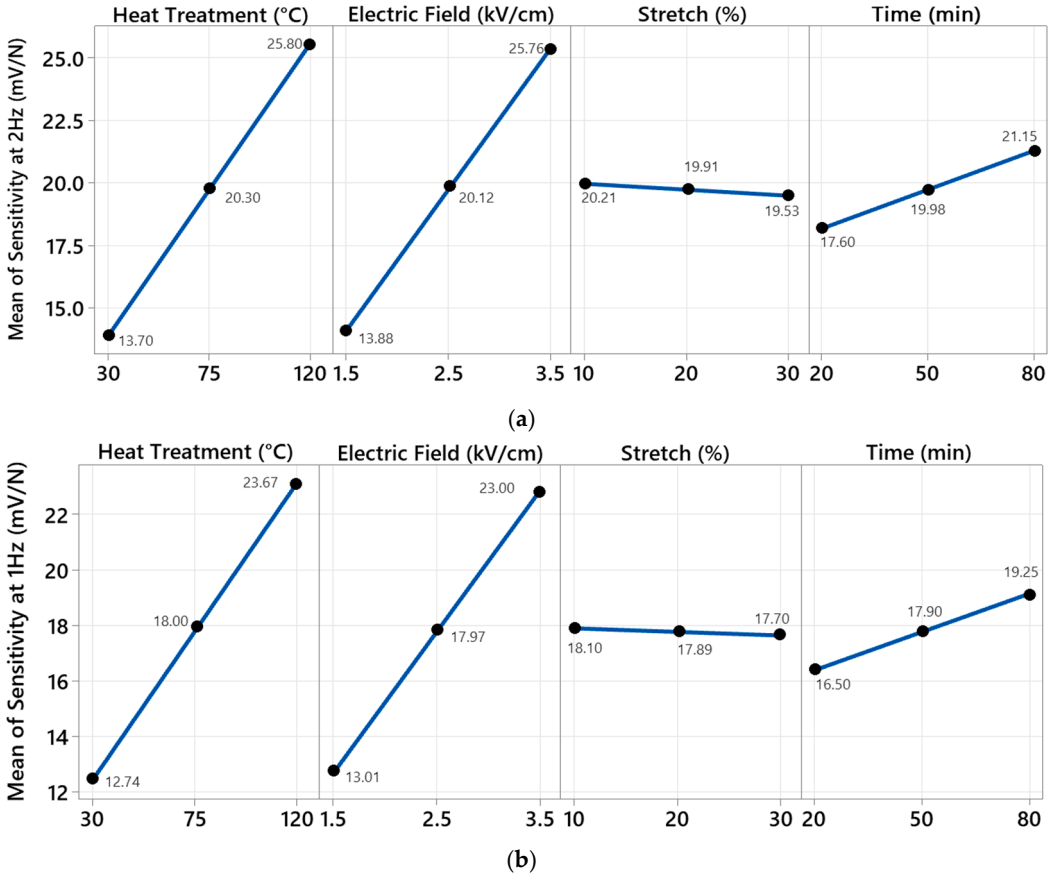

Figure 17. *Cont.*

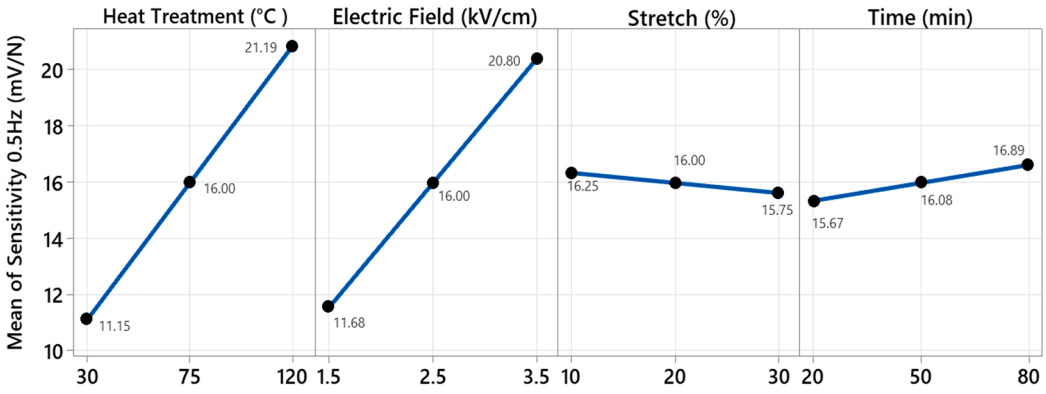

(**c**)

Figure 17. Main effect plots obtained from definitive screen design analysis for the sensitivity of PVDF electrospun sensors (**a**) at 2Hz, (**b**) at 1Hz, (**c**) at 0.5Hz.

This observation can be attributed to the stretching of PVDF polymer chains during electrospinning, which is when the nanofibers are formed. The high electric field during electrospinning and the rapid movement of the drum surface where the fibers are deposited lead to the significant stretching of the nanofibers. After this initial stretching, further stretching has little impact on polarization or the increase in the β-phase. Instead, excessive stretching can cause nanofiber breakage and weaken the mat [62].

The values of the piezoelectric voltage coefficient (g_{33}) and piezoelectric charge coefficient (d_{33}) were obtained from Equations (7) and (8) [63,64], where V = voltage, L = length of the sensor, w = width of the sensor, F = force, t = thickness, $\mathcal{E}'$ = relative permittivity of the sample, and ε_o = the vacuum permittivity (8.85×10^{-12} Fm^{-1}).

$$g_{33} = \frac{V \times L \times w}{F \times t} \tag{7}$$

$$g_{33} = \frac{d_{33}}{\varepsilon' \times \varepsilon_o} \tag{8}$$

Table 4 shows the comparison of the β-phase, g_{33} and d_{33} reported by many researchers and the data obtained in this study.

Table 4. Comparison of the β-phase, piezoelectric voltage coefficient (g_{33}), and piezoelectric charge coefficient (d_{33}) of the polarized and non-polarized samples.

Sample	β-Phase (%)	g_{33} (mV m/N)			d_{33}		
		at 2 Hz	at 1 Hz	at 0.5 Hz	at 2 Hz	at 1 Hz	at 0.5 Hz
EP-3	85	10	7.8	5.5	2.4	1.8	1.3
EP-4	89	23.2	22.01	20.9	6	5.68	5.4
EP-5	95	39	32	27	10	8.5	7.34
EP-11	81	5.6	4.9	3.3	1.3	1.0	0.75
Non-polarized PVDF (P)	75	4.8	3.4	2.7	1.1	0.76	0.62
PVDF film in the literature	30–50 [65,66]	4.5 mV m/N Quasi-static testing [67]			6 pC/N static testing [23] 2.5 pC/N Quasi-static testing (thickness of 0.6 mm) [67]		
Electrically poled PVDF in the literature	70–81 [68]	0.06 V m/N at 110 Hz loading frequency and poled at 75 kV/mm [69]			6–8 pC/N depending on the temperature of measurements during Quasi-static testing (Poled at 150 MV/m) [70] 10 pC/N when poled at 300 kV/cm Quasi-static testing [28]		

A key challenge in introducing these sensors to the commercial market is ensuring their long-term durability, consistent signal generation over time, and overall sensor lifespan. In future work, the plan is to investigate the long-term durability of PVDF-based sensors by utilizing thin-film-coated electrodes on electrospun mats, which will improve electrode adhesion and enhance robustness. Additionally, we will explore the effects of various encapsulating materials on the ability of PVDF to generate signals to identify optimal solutions for sensor performance and longevity.

4. Conclusions

In conclusion, optimizing the % F(β) and sensitivity of PVDF films requires the careful balancing of the heat treatment temperature, electric field, % stretch, and polarization time. Achieving the desired F(β) is crucial for enhancing the material's piezoelectric properties. In this study, an electrospun mat of PVDF was subjected to heat treatment and electrical polarization following a statistical design of experiments. The ability of electrically polarized PVDF nanofiber mats to generate voltage was measured under a force ranging between 1 and 10 N and very low-frequency conditions (0.5–2 Hz). An increase in % F(β) from 75% (non-polarized electrospun PVDF mat) to 95% (polarized electrospun PVDF mat) was observed after applying a 3.5 kV/cm electric field for 80 min at 120 °C under a 20% stretch. The findings of this work indicate that both the temperature and electric field significantly influence % F(β), with higher values being achieved at elevated conditions. The highly polarized samples offered sensitivities of 35 mV/N, 29 mV/N, and 22 mV/N at 2 Hz, 1 Hz, and 0.5 Hz, respectively. The % stretch effect was almost negligible due to the polymer chains being adequately stretched during electrospinning, under the influence of a high electric field, and during fiber collection on the drum. It is well documented in the literature [71] that the g_{33} tends to decrease significantly at low frequencies, limiting the efficiency of energy conversion when force is applied. This work reports g_{33} values of 39 mV·m/N at 2 Hz, 32 mV·m/N at 1 Hz, and 27 mV·m/N at 0.5 Hz, demonstrating the potential of electrospun polarized PVDF to be used in low-frequency sensor applications.

Author Contributions: Conceptualization, A.T. and A.H.B.; Methodology, A.T. and M.T.; Software, A.T.; Formal analysis, A.T.; Investigation, A.H.B.; Writing—original draft, A.T.; Writing—review & editing, G.R.; Supervision, G.R.; Project administration, G.R.; Funding acquisition, G.R. All authors have read and agreed to the published version of the manuscript.

Funding: This research was supported by funds provided by the Natural Sciences and Engineering Research Council of Canada (NSERC) under project DDG-2023-00033.

Data Availability Statement: The data used to support the findings of this study are included within the article.

Acknowledgments: The authors express their gratitude to Walter Sebastian, Uta Helbig, and Jens Helbig at The Technische Hochschule Nürnberg Georg Simon Ohm, Germany, for sharing knowledge and letting us use lab equipment for the dielectric characterization. In addition, we are thankful to Jewgeni Roudenko and Olaf Kottas at Technische Hochschule Nürnberg Georg Simon Ohm, Germany, for helping us with the analysis of the material.

Conflicts of Interest: The authors declare no conflict of interest.

References

1. Mirjalili, S.; Tohidi Moghadam, T.; Sajedi, R.H. Facile and Rapid Detection of Microalbuminuria by Antibody-Functionalized Gold Nanorods. *Plasmonics* **2022**, *17*, 1269–1277. [CrossRef]
2. Ding, Y.; Onyilagha, O.; Zhu, Z. 9—Electrospun nanofibers for tactile sensors. In *Functional Tactile Sensors*; Zhou, Y., Chou, H.-H., Eds.; Woodhead Publishing: Sawston, UK, 2021; pp. 159–196.

3. Zhu, C.; Zheng, J.; Fu, J. Electrospinning Nanofibers as Stretchable Sensors for Wearable Devices. *Macromol. Biosci.* **2024**, *24*, 2300274. [CrossRef] [PubMed]
4. Wang, Y.; Yokota, T.; Someya, T. Electrospun nanofiber-based soft electronics. *NPG Asia Mater.* **2021**, *13*, 22. [CrossRef]
5. Li, Y.; Abedalwafa, M.A.; Tang, L.; Li, D.; Wang, L. Chapter 18—Electrospun Nanofibers for Sensors. In *Electrospinning: Nanofabrication and Applications*; Ding, B., Wang, X., Yu, J., Eds.; William Andrew Publishing: Norwich, NY, USA, 2019; pp. 571–601.
6. Mondal, K.; Sharma, A. Recent advances in electrospun metal-oxide nanofiber based interfaces for electrochemical biosensing. *RSC Adv.* **2016**, *6*, 94595–94616. [CrossRef]
7. Hsu, Y.-C.; Wu, C.-C.; Lee, C.-C.; Cao, G.; Shen, I. Demonstration and characterization of PZT thin-film sensors and actuators for meso-and micro-structures. *Sens. Actuators A Phys.* **2004**, *116*, 369–377. [CrossRef]
8. Smith, G.L.; Pulskamp, J.S.; Sanchez, L.M.; Potrepka, D.M.; Proie, R.M.; Ivanov, T.G.; Rudy, R.Q.; Nothwang, W.D.; Bedair, S.S.; Meyer, C.D. PZT-based piezoelectric MEMS technology. *J. Am. Ceram. Soc.* **2012**, *95*, 1777–1792. [CrossRef]
9. Chen, B.; Li, H.; Tian, W.; Zhou, C. PZT based piezoelectric sensor for structural monitoring. *J. Electron. Mater.* **2019**, *48*, 2916–2923. [CrossRef]
10. Wang, X.; Zhou, J.; Song, J.; Liu, J.; Xu, N.; Wang, Z.L. Piezoelectric field effect transistor and nanoforce sensor based on a single ZnO nanowire. *Nano Lett.* **2006**, *6*, 2768–2772. [CrossRef]
11. Tan, Y.; Yang, K.; Wang, B.; Li, H.; Wang, L.; Wang, C. High-performance textile piezoelectric pressure sensor with novel structural hierarchy based on ZnO nanorods array for wearable application. *Nano Res.* **2021**, *14*, 3969–3976. [CrossRef]
12. Duan, S.; Wu, J.; Xia, J.; Lei, W. Innovation Strategy Selection Facilitates High-Performance Flexible Piezoelectric Sensors. *Sensors* **2020**, *20*, 2820. [CrossRef] [PubMed]
13. Li, X.; Zhang, Z.; Peng, Z.; Yan, X.; Hong, Y.; Liu, S.; Lin, W.; Shan, Y.; Wang, Y.; Yang, Z. Fast and versatile electrostatic disc microprinting for piezoelectric elements. *Nat. Commun.* **2023**, *14*, 6488. [CrossRef] [PubMed]
14. Ai, Y.; Gu, Z.X.; Wang, P.; Tang, Y.Y.; Chen, X.G.; Lv, H.P.; Li, P.F.; Jiang, Q.; Xiong, R.G.; Zhang, J.J.; et al. Biodegradable Ferroelectric Molecular Plastic Crystal HOCH(2)(CF(2))(7)CH(2)OH Structurally Inspired by Polyvinylidene Fluoride. *Adv. Mater.* **2024**, *36*, e2405981. [CrossRef] [PubMed]
15. Wan, X.; Cong, H.; Jiang, G.; Liang, X.; Liu, L.; He, H. A review on PVDF nanofibers in textiles for flexible piezoelectric sensors. *ACS Appl. Nano Mater.* **2023**, *6*, 1522–1540. [CrossRef]
16. Nalwa, H.S. *Ferroelectric Polymers: Chemistry: Physics, and Applications*; CRC Press: Boca Raton, FL, USA, 1995.
17. Lovinger, A.J.; Furukawa, T.; Davis, G.; Broadhurst, M. Crystallographic changes characterizing the Curie transition in three ferroelectric copolymers of vinylidene fluoride and trifluoroethylene: 1. As-crystallized samples. *Polymer* **1983**, *24*, 1225–1232. [CrossRef]
18. Kaur, S.; Kumar, A.; Sharma, A.L.; Singh, D.P. Influence of annealing on dielectric and polarization behavior of PVDF thick films. *J. Mater. Sci. Mater. Electron.* **2017**, *28*, 8391–8396. [CrossRef]
19. Lovinger, A.J. Annealing of poly (vinylidene fluoride) and formation of a fifth phase. *Macromolecules* **1982**, *15*, 40–44. [CrossRef]
20. Roopa, T.; Murthy, H.N.; Harish, D.; Jain, A.; Angadi, G. Properties of PVDF films stretched in machine direction. *Polym. Polym. Compos.* **2021**, *29*, 198–206. [CrossRef]
21. Zhu, Y.; Ye, H.; Yang, L.; Jiang, L.; Zhen, L.; Huang, J.; Jiao, Z.; Sun, J. Effect of annealing temperatures and time on structural evolution and dielectric properties of PVDF films. *Polym. Polym. Compos.* **2016**, *24*, 167–172. [CrossRef]
22. Riquelme, S.A.; Ramam, K. Dielectric and piezoelectric properties of lead free BZT-BCT/PVDF flexible composites for electronic applications. *Mater. Res. Express* **2019**, *6*, 116331. [CrossRef]
23. Zhang, C.; Sun, H.; Zhu, Q. Preparation and Property Enhancement of Poly(Vinylidene Fluoride) (PVDF)/Lead Zirconate Titanate (PZT) Composite Piezoelectric Films. *J. Electron. Mater.* **2021**, *50*, 6426–6437. [CrossRef]
24. Ye, Y.; Jiang, Y.; Wu, Z.; Zeng, H. Phase transitions of poly (vinylidene fluoride) under electric fields. *Integr. Ferroelectr.* **2006**, *80*, 245–251. [CrossRef]
25. Nasef, M.M.; Saidi, H.; Dahlan, K.Z.M. Investigation of electron irradiation induced-changes in poly (vinylidene fluoride) films. *Polym. Degrad. Stab.* **2002**, *75*, 85–92. [CrossRef]
26. Huang, Y.-Z.; Liu, Z.; Li, L.-W.; He, H.-Z.; Wang, Z.L.; Qu, J.-P.; Chen, X.; Huang, Z.-X. Giant Piezoelectric Coefficient of Polyvinylidene Fluoride with Rationally Engineered Ultrafine Domains Achieved by Rapid Freezing Processing. *Adv. Mater.* **2024**, e2412344. [CrossRef]
27. Salimi, A.; Yousefi, A. Analysis method: FTIR studies of β-phase crystal formation in stretched PVDF films. *Polym. Test.* **2003**, *22*, 699–704. [CrossRef]
28. Debili, S.; Gasmi, A.; Bououdina, M. Synergistic effects of stretching/polarization temperature and electric field on phase transformation and piezoelectric properties of polyvinylidene fluoride nanofilms. *Appl. Phys. A* **2020**, *126*, 309. [CrossRef]
29. Qin, S.; Zhang, X.; Yu, Z.; Zhao, F. Polarization study of poly(vinylidene fluoride) films under cyclic electric fields. *Polym. Eng. Sci.* **2020**, *60*, 645–656. [CrossRef]

30. Pang, Z.; Li, Y.; Zheng, H.; Qin, R. Microscopic Mechanism of Electrical Aging of PVDF Cable Insulation Material. *Polymers* **2023**, *15*, 1286. [CrossRef]
31. Chatterjee, A.; Das, A.; Saha, K.; Jeong, U. Nanofiller-Induced Enhancement of PVDF Electroactivity for Improved Sensing Performance. *Adv. Sensor Res.* **2023**, *2*, 2200080. [CrossRef]
32. Bhattacharya, D.; Bayan, S.; Mitra, R.K.; Ray, S.K. Flexible Biomechanical Energy Harvesters with Colossal Piezoelectric Output (∼2.07 V/kPa) Based on Transition Metal Dichalcogenides-Poly (vinylidene fluoride) Nanocomposites. *ACS Appl. Electron. Mater.* **2020**, *2*, 3327–3335. [CrossRef]
33. Sasmal, A.; Patra, A.; Devi, P.S.; Sen, S. Hydroxylated $BiFeO_3$ as efficient fillers in poly (vinylidene fluoride) for flexible dielectric, ferroelectric, energy storage and mechanical energy harvesting application. *Dalton Trans.* **2021**, *50*, 1824–1837. [CrossRef] [PubMed]
34. Parker, A.; Ueda, A.; Marvinney, C.; Hargrove, S.; Williams, F.; Mu, R. Structural and thermal treatment evaluation of electrospun PVDF nanofibers for sensors. *J. Polym. Sci. Appl.* **2018**, *2*, 1–4.
35. Tariq, A.; Behravesh, A.H.; Utkarsh; Rizvi, G. Statistical Modeling and Optimization of Electrospinning for Improved Morphology and Enhanced β-Phase in Polyvinylidene Fluoride Nanofibers. *Polymers* **2023**, *15*, 4344. [CrossRef] [PubMed]
36. Kaura, T.; Nath, R.; Perlman, M. Simultaneous stretching and corona poling of PVDF films. *J. Phys. D Appl. Phys.* **1991**, *24*, 1848. [CrossRef]
37. Ghafari, E.; Lu, N. Self-polarized electrospun polyvinylidene fluoride (PVDF) nanofiber for sensing applications. *Compos. Part B Eng.* **2019**, *160*, 1–9. [CrossRef]
38. Fortunato, M.; Tamburrano, A.; Bracciale, M.P.; Santarelli, M.L.; Sarto, M.S. Enhancement of the piezoelectric coefficient in PVDF-TrFe/$CoFe_2O_4$ nanocomposites through DC magnetic poling. *Beilstein J. Nanotechnol.* **2021**, *12*, 1262–1270. [CrossRef]
39. Zhu, R.; Wang, Z. 9—Piezoelectric one- to two-dimensional nanomaterials for vibration energy harvesting devices. In *Emerging 2D Materials and Devices for the Internet of Things*; Tao, L., Akinwande, D., Eds.; Elsevier: Amsterdam, The Netherlands, 2020; pp. 221–241.
40. Lang, C.; Fang, J.; Shao, H.; Ding, X.; Lin, T. High-sensitivity acoustic sensors from nanofibre webs. *Nat. Commun.* **2016**, *7*, 11108. [CrossRef]
41. Ghasemi-Mobarakeh, L.; Semnani, D.; Morshed, M. A novel method for porosity measurement of various surface layers of nanofibers mat using image analysis for tissue engineering applications. *J. Appl. Polym. Sci.* **2007**, *106*, 2536–2542. [CrossRef]
42. Kalimuldina, G.; Turdakyn, N.; Abay, I.; Medeubayev, A.; Nurpeissova, A.; Adair, D.; Bakenov, Z. A review of piezoelectric PVDF film by electrospinning and its applications. *Sensors* **2020**, *20*, 5214. [CrossRef]
43. Hosseini, S.M.; Yousefi, A.A. Piezoelectric sensor based on electrospun PVDF-MWCNT-Cloisite 30B hybrid nanocomposites. *Org. Electron.* **2017**, *50*, 121–129. [CrossRef]
44. Samadi, A.; Hosseini, S.M.; Mohseni, M. Investigation of the electromagnetic microwaves absorption and piezoelectric properties of electrospun Fe_3O_4-GO/PVDF hybrid nanocomposites. *Org. Electron.* **2018**, *59*, 149–155. [CrossRef]
45. Cho, S.; Lee, J.S.; Jang, J. Poly (vinylidene fluoride)/NH2-treated graphene nanodot/reduced graphene oxide nanocomposites with enhanced dielectric performance for ultrahigh energy density capacitor. *ACS Appl. Mater. Interfaces* **2015**, *7*, 9668–9681. [CrossRef]
46. Satthiyaraju, M.; Ramesh, T. Effect of annealing treatment on PVDF nanofibers for mechanical energy harvesting applications. *Mater. Res. Express.* **2019**, *6*, 105366. [CrossRef]
47. Li, H.; Ye, L.; Zhang, Y.; Ran, C.; Yan, T.; Liao, H.; Zhang, J.; Ma, S. Effects of heat treatment on the dielectric and energy storage properties of BT-PVDF nanocomposite films. *Polym. Compos.* **2024**, *45*, 3010–3018. [CrossRef]
48. Martins, P.; Lopes, A.C.; Lanceros-Mendez, S. Electroactive phases of poly(vinylidene fluoride): Determination, processing and applications. *Prog. Polym. Sci.* **2014**, *39*, 683–706. [CrossRef]
49. Gowdhaman, P.; Annamalai, V.; Thakur, O. Piezo, ferro and dielectric properties of ceramic-polymer composites of 0–3 connectivity. *Ferroelectrics* **2016**, *493*, 120–129. [CrossRef]
50. Chamankar, N.; Khajavi, R.; Yousefi, A.A.; Rashidi, A.; Golestanifard, F. An experimental model for predicting the piezo and dielectric constant of PVDF-PZT nanocomposite fibers with 0–3 and 1–3 connectivity. *Ceram. Int.* **2020**, *46*, 23567–23581. [CrossRef]
51. Laschuk, N.O.; Easton, E.B.; Zenkina, O.V. Reducing the resistance for the use of electrochemical impedance spectroscopy analysis in materials chemistry. *RSC Adv.* **2021**, *11*, 27925–27936. [CrossRef]
52. Khair, M.; Rashid, M.R.; Ahmed, S.; Susan, M.A.B.H. Silica fillers for enhancement of dielectric properties of poly (vinylidene fluoride) and its copolymer. *Mater. Today Proc.* **2020**, *29*, 1239–1245. [CrossRef]
53. Dahan, R.; Arshad, A.; Hafiz, M.; Zulkefle, H.; Ismail, L.; Muhamad, N.; Rusop, M. Dielectric constant of PVDF/MgO nanocomposites thin films. In Proceedings of the 2012 IEEE Symposium on Business, Engineering and Industrial Applications, Bandung, Indonesia, 23–26 September 2012; pp. 18–22.
54. Li, Y.; Krentz, T.M.; Wang, L.; Benicewicz, B.C.; Schadler, L.S. Ligand engineering of polymer nanocomposites: From the simple to the complex. *ACS Appl. Mater. Interfaces* **2014**, *6*, 6005–6021. [CrossRef]

55. Wang, Q.; Che, J.; Wu, W.; Hu, Z.; Liu, X.; Ren, T.; Chen, Y.; Zhang, J. Contributing Factors of Dielectric Properties for Polymer Matrix Composites. *Polymers* **2023**, *15*, 590. [CrossRef] [PubMed]
56. Qiu, J.; Gu, Q.; Sha, Y.; Huang, Y.; Zhang, M.; Luo, Z. Preparation and application of dielectric polymers with high permittivity and low energy loss: A mini review. *J. Appl. Polym. Sci.* **2022**, *139*, 52367. [CrossRef]
57. Bruggeman, V.D. Berechnung verschiedener physikalischer Konstanten von heterogenen Substanzen. I. Dielektrizitätskonstanten und Leitfähigkeiten der Mischkörper aus isotropen Substanzen. *Ann. Der Phys.* **1935**, *416*, 636–664. [CrossRef]
58. Sihvola, A.H. *Electromagnetic Mixing Formulas and Applications*; IET: London, UK, 1999.
59. Šutka, A.; Sherrell, P.C.; Shepelin, N.A.; Lapčinskis, L.; Mālnieks, K.; Ellis, A.V. Measuring Piezoelectric Output—Fact or Friction? *Adv. Mater.* **2020**, *32*, 2002979. [CrossRef]
60. Yong, Y.K.; Fleming, A.J. Note: An improved low-frequency correction technique for piezoelectric force sensors in high-speed nanopositioning systems. *Rev. Sci. Instrum.* **2017**, *88*, 046105. [CrossRef] [PubMed]
61. Ruan, L.; Yao, X.; Chang, Y.; Zhou, L.; Qin, G.; Zhang, X. Properties and Applications of the β Phase Poly(vinylidene fluoride). *Polymers* **2018**, *10*, 228. [CrossRef] [PubMed]
62. Sencadas, V.; Gregorio, R., Jr.; Lanceros-Méndez, S. α to β Phase Transformation and Microestructural Changes of PVDF Films Induced by Uniaxial Stretch. *J. Macromol. Sci. Part B* **2009**, *48*, 514–525. [CrossRef]
63. Clark, W.W.; Mo, C. Piezoelectric energy harvesting for bio mems applications. In *Energy Harvesting Technologies*; Springer: Berlin/Heidelberg, Germany, 2009; pp. 405–430.
64. Parjansri, P.; Intatha, U.; Guo, R.; Bhalla, A.; Eitssayeam, S. Effect of Sb_2O_3 on the electrical properties of $Ba_{0.9}Ca_{0.1}Zr_{0.1}Ti_{0.9}O_3$ ceramics fabricated using nanocrystals seed. *Appl. Phys. A* **2016**, *122*, 840. [CrossRef]
65. Wang, A.; Chen, C.; Liao, L.; Qian, J.; Yuan, F.-G.; Zhang, N. Enhanced β-Phase in Direct Ink Writing PVDF Thin Films by Intercalation of Graphene. *J. Inorg. Organomet. Polym. Mater.* **2020**, *30*, 1497–1502. [CrossRef]
66. Hu, P.; Yan, L.; Zhao, C.; Zhang, Y.; Niu, J. Double-layer structured PVDF nanocomposite film designed for flexible nanogenerator exhibiting enhanced piezoelectric output and mechanical property. *Compos. Sci. Technol.* **2018**, *168*, 327–335. [CrossRef]
67. Li, R.; Zhou, J.; Liu, H.; Pei, J. Effect of Polymer Matrix on the Structure and Electric Properties of Piezoelectric Lead Zirconatetitanate/Polymer Composites. *Materials* **2017**, *10*, 945. [CrossRef]
68. Yasar, M.; Hassett, P.; Murphy, N.; Ivankovic, A. β Phase Optimization of Solvent Cast PVDF as a Function of the Processing Method and Additive Content. *ACS Omega* **2024**, *9*, 26020–26029. [CrossRef] [PubMed]
69. Kaeopisan, A.; Thanachayanon, C.; Wattanasarn, H. Tunable α-γ-phase of polyvinylidene fluoride to enhance piezoelectric coefficient. *J. Polym. Res.* **2022**, *29*, 235. [CrossRef]
70. Zhou, Y.; Liu, J.; Hu, X.; Chu, B. Apparent piezoelectric response from the bending of non-poled PVDF. *Appl. Phys. Express* **2019**, *12*, 061006. [CrossRef]
71. Heywang, W.; Lubitz, K.; Wersing, W. *Piezoelectricity: Evolution and Future of a Technology*; Springer Science & Business Media: Berlin/Heidelberg, Germany, 2008; Volume 114.

Disclaimer/Publisher's Note: The statements, opinions and data contained in all publications are solely those of the individual author(s) and contributor(s) and not of MDPI and/or the editor(s). MDPI and/or the editor(s) disclaim responsibility for any injury to people or property resulting from any ideas, methods, instructions or products referred to in the content.